PHYSICAL REVIEW B **84**, 205424 (2011)

Electron transmission through atomic steps of Bi_2Se_3 and Bi_2Te_3 surfaces

Katsuyoshi Kobayashi
Department of Physics, Faculty of Science, Ochanomizu University, 2-1-1 Otsuka, Bunkyo-ku, Tokyo 112-8610, Japan

(Received 14 September 2011; revised manuscript received 24 October 2011; published 15 November 2011)

Transmission properties of surface-state electrons through steps of Bi_2Se_3 and Bi_2Te_3 surfaces are theoretically studied with a tight-binding method. Transmission spectra of Bi_2Se_3 as a function of the incident angle are simply explained in terms of potential scattering of a massless Dirac Hamiltonian. However, those of Bi_2Te_3 are not similarly explained, and perfect reflection appears at an angle. The mechanism of perfect reflection is discussed in terms of the massless Dirac Hamiltonian with the hexagonal-warping term. It is found that evanescent waves generated by the hexagonal-warping term are the origin of the perfect reflection, which is similar to bilayer graphene.

DOI: 10.1103/PhysRevB.84.205424 PACS number(s): 73.20.At, 73.25.+i, 72.10.Fk

I. INTRODUCTION

The topological insulator is a new type of classification of insulators. A number of studies on this subject have been made, and many interesting properties have been revealed.[1–4]

A characteristic feature of topological insulators is the existence of topological surface states. Electrons in the surface states are not scattered in the backward direction by scatterers with time-reversal symmetry. This is due to the property that the surface-state electrons traveling in the opposite directions with the same spin orientation are localized on the opposite surfaces of materials, and they are spatially separated. Evidence of the absence of backward scattering has been given by experiments using scanning tunneling spectroscopy (STS).[5–8] We present a theoretical study on electron transmission through surface steps of Bi_2Se_3 and Bi_2Te_3.

We choose Bi_2Se_3 and Bi_2Te_3 in this study because it is shown by density-functional calculations[9–11] and angle-resolved photoemission spectroscopy (ARPES)[10,12] that these materials are three-dimensional strong topological insulators with single Dirac cones on the surfaces. We study the transmission through steps because a step is a one-dimensional scatterer which is suitable for discussing directly the absence of backward scattering. Transmission probability through steps has been measured by STS for Sb surfaces.[8] The standing waves formed by surface steps have been observed on the Bi_2Te_3 surface[6,7,13] and the Bi_2Se_3 surface.[13]

There have been several theoretical studies on the scattering by steps and point defects using the effective Hamiltonian for surface states[14–17] or a model lattice Hamiltonian with four bands.[18] In contrast to these studies we present numerical results of the electron transmission through steps calculated using atomistic models. A step is a change in boundary condition or bonding configuration. It is not clear whether the scattering by steps is effectively expressed by a potential in a two-dimensional Hamiltonian neglecting the spatial variation of wave functions in the direction normal to surfaces. The Dirac cones of Bi_2Se_3 and Bi_2Te_3 are confined in narrow regions near the center of the two-dimensional Brillouin zone. Therefore the wave length of the surface states is much larger than the atom spacing in the directions parallel to surfaces. However, the decay lengths of wave functions of the surface states are atomic scales, and they are comparable with the step heights of atomic steps. Therefore, for discussing the validity of effective models and analyzing experimental results, it is necessary to calculate the transmission through steps with taking account of the atomistic character of Bi_2Se_3 and Bi_2Te_3.

In this paper we use a tight-binding model. The tight-binding parameters are determined by fitting to the band structures obtained by density-functional calculations. We calculate the transmission probability through steps as a function of the incident angle with respect to the step line. We find a distinct difference in transmission spectra between Bi_2Se_3 and Bi_2Te_3. Perfect reflection exists in Bi_2Te_3. The perfect reflection is explained by the hexagonal-warping term added to the massless Dirac Hamiltonian,[19] where evanescent waves play an important role. The mechanism is similar to that of the bilayer graphene.[20]

II. METHOD OF CALCULATIONS

We use a tight-binding method for expressing electronic states. The tight-binding parameters are determined by fitting to band structures obtained by density-functional calculations. We take account of the transfer between third-nearest-neighbor atoms. The spin-orbital interaction is taken into account in the intra-atomic matrix elements.[21] Details of the tight-binding calculation are shown in the Appendix.

In the experiments of standing waves it is confirmed that steps run along the close-packing $[1\bar{1}0]$ direction, but the atomic structures of steps are not determined.[6,7,13] Therefore, we assume the step structures shown in Figs. 1 and 2. The atomic structures of Bi_2Se_3 and Bi_2Te_3 are ABC stacking of layers with the hexagonal lattice. A unit of the layered structure is a quintuple layer (QL) of Se-Bi-Se-Bi-Se, for example. We consider steps with heights of one QL or two QLs.

The side surfaces of steps run along the sequence of the ABC stacking as shown in Fig. 1. We consider two side surfaces labeled by steps I and II. The side surfaces of steps I and II are (221) and (334) surfaces, and they give steep and gentle slopes, respectively. Each atom in the bulk structures has three nearest-neighbor atoms in the neighboring layers. For the atoms on the side surfaces of the steps, the number of neighboring atoms in the upper layers is two and one in steps I and II, respectively. Therefore, it is expected that step I has larger stability than step II. The side surface of step I is the close-packing surface if the crystal structure is

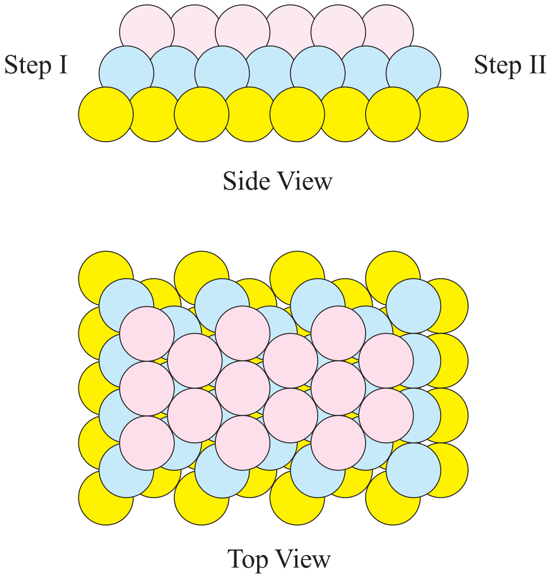

FIG. 1. (Color online) Atomic structure of steps.

face-centered cubic. It is the same surface as that studied by a density-functional method in Ref. 22.

We do not consider the reconstruction of the atomic structures of steps. We consider the step structures obtained by introducing slips into slabs on the side surfaces as shown in Fig. 2. We calculate transmission probability for four step structures. One is the step I structure with single QL height. Second is the same structure with double QL height. Third is the step II structure with single QL height. And fourth is the same as the first one with a slip in the reverse direction. We use the same tight-binding parameters for the step structures as those for the flat surfaces. Real steps may have reconstruction and calculated results may change accordingly. However, transmission calculations show general properties that do not depend on the individual step structure as shown in Sec. III.

Transmission probability is calculated by the usual method shown in Ref. 23. We consider slabs with a finite thickness shown in Fig. 2. The slabs infinitely extend in the directions parallel to the surfaces. Electrons coming, for example, from the left side are scattered at the steps. Some are transmitted to the right side and others are reflected to the left side. We separate the slabs into incident, scattering, and transmitted regions, and solve the scattering problem by two steps. In the first step we solve all Bloch states including propagating and evanescent waves in the incident and transmitted regions for fixed energy. In the second step we impose the boundary condition with a single incoming wave and all out-going waves on the tight-binding equation in the scattering region. This changes the tight-binding equation for the slabs with the infinite extent in the surface parallel directions into a linear equation closed within the scattering region. The transmission and reflection probabilities are obtained by solving the linear equation.

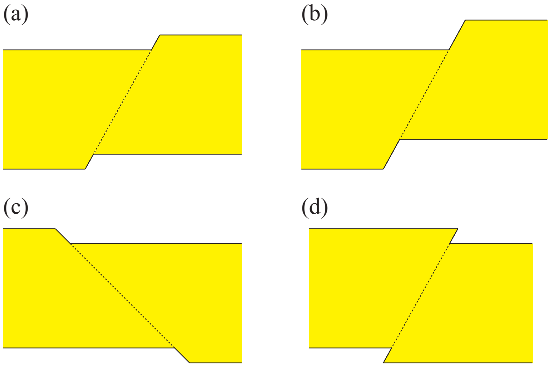

FIG. 2. (Color online) Step structures. (a) Step I with single QL height, (b) step I with double QL height, (c) step II with single QL height, and (d) the same as (a) with a slip in the reverse direction.

In the present calculation we assume the simple step structures made by inserting a slip into a flat slab as shown in Fig. 2. Therefore, in principle, we can take the region with one atomic-layer thickness in both sides of the slip plane as the narrowest scattering region. However, we did not obtain results with good numerical accuracy from calculations using the narrowest scattering region. The reason is as follows. A wave function of a scattering state consists of propagating and evanescent waves. When the scattering region is narrow, evanescent waves do not much decay in the scattering region. The amplitude of the rapidly decaying evanescent waves is not small at the boundary of the scattering region. This means that accurate boundary conditions for the rapidly decaying components are required to obtain an accurate wave function in the scattering region. However, it is generally difficult to obtain numerically accurate wave functions and decay constants of the rapidly decaying evanescent waves. Therefore, inaccuracy in giving boundary conditions for rapidly decaying components is the origin of errors in calculating transmission properties.

A simple way to eliminate the numerical errors is to take wide scattering regions as proposed in Ref. 24. The rapidly decaying evanescent waves fully decay in wide scattering regions. The transmission properties do not depend on the boundary conditions for the rapidly decaying components. Therefore we obtain accurate transmission properties even with inaccurate boundary conditions for the rapidly decaying components. We found that numerical accuracy is improved when we use scattering regions with from 10 to 15 atomic cells in width in a direction parallel to the surface of the slab.

III. CALCULATED RESULTS

A. Bi_2Se_3

Figure 3 shows calculated transmission probability through a surface step of Bi_2Se_3. Transmission probability is calculated for the step I structure with single QL step height shown in Fig. 2(a). The thickness of the slab is varied from 2 to 5 QLs. The spectra are calculated as a function of energy for the normal incidence to the step line. Since slabs with finite thicknesses are used, there are two channels of right-going surface states. One is localized on the upper surface, and the other is localized on the lower surface of the slabs. Therefore, the energy regions where the number of channels is two near zero energy show the transmission of surface states. The band structure for each slab without steps is also shown. $\bar{\Gamma}$, $\bar{K}$, $\bar{M}$ are the center, a corner, and the middle point of a side of

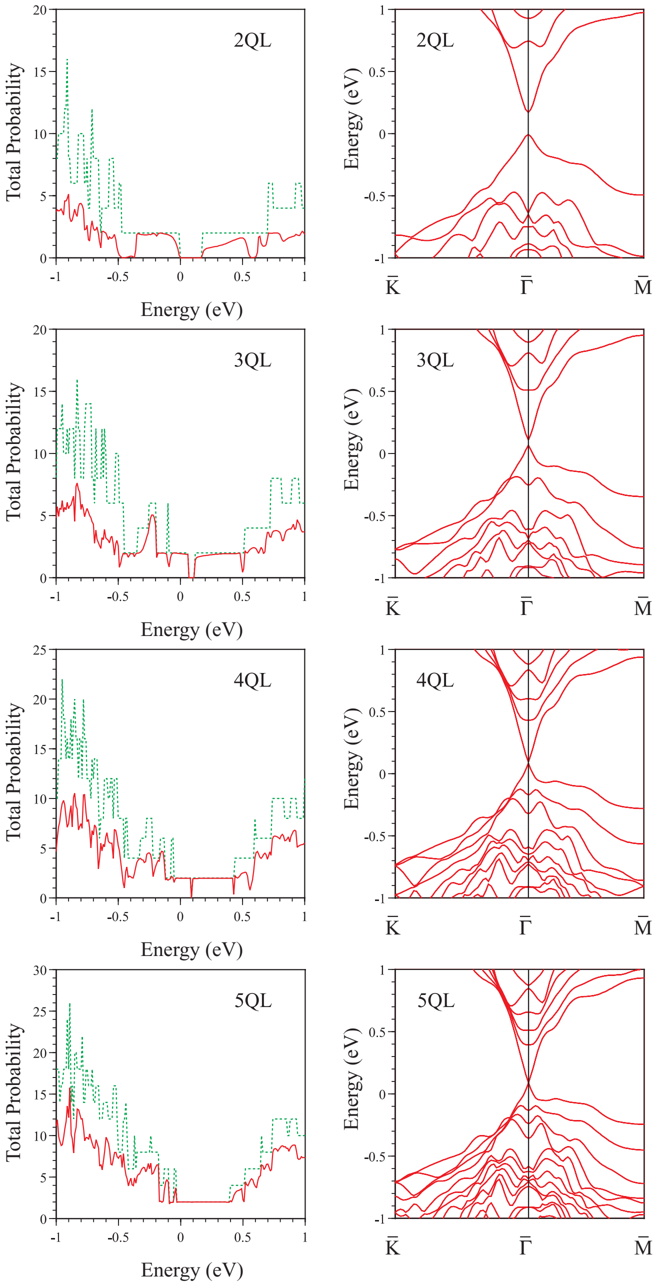

FIG. 3. (Color online) Total transmission probability through a 1QL step of Bi_2Se_3 thin films as a function of energy. Probability is calculated for normal incidence to the step line. Solid and dotted lines show transmission probability and the number of transmission channels, respectively. The band structures of thin films without steps are also shown on the right side.

the hexagonal Brillouin zone, respectively. The step line runs parallel to the $\bar{\Gamma}$-$\bar{K}$ direction.

The band gaps of surface states are clearly seen in the 2 and 3 QL slabs at the $\bar{\Gamma}$ point near zero energy. This is due to the interaction between the surface states localized on the two surfaces of the slabs. The corresponding gaps are also seen in the transmission spectra, and the transmission deviates from the perfect one in the energy regions near the gaps. The occurrence of reflection may be interpreted as that an electron in the right-going surface state localized on the upper surface of a slab is scattered by steps to the left-going surface state localized on the lower surface. The reflection decreases with decreasing the gap. The gap is very small for the 4 and 5 QL slabs, and the transmission of surface states is almost perfect. The present calculation suggests that 5 QLs are sufficient for observing the perfect transmission property for surface states.

Outside of the energy regions of surface states, the transmission is not perfect. This is due to the fact that current is carried by bulk states. Since bulk states extend over the slabs, the effect of steps on transmission decreases with increasing the thickness of slabs. Therefore the transmission probability increases with increasing the thickness.

Next we show the angular dependence of transmission with respect to the step line for the 5 QL slab. Figure 4 shows transmission probability as a function of the wave number parallel to the step line. Energy is 0.2 eV. Only surface states exist at this energy. Transmission probability is calculated for the four step structures shown in Fig. 2.

The transmission is perfect at zero wave number. The transmission probability monotonically decreases with increasing the wave number, and reaches zero at the maximum wave number of propagating waves. This characteristic is common to the various types of step structures of Bi_2Se_3. The transmission through the double QL step slightly deviates from the perfect one at zero wave number. This is due to the fact that the constricted part of the slab by double QL steps is narrower than those by single QL steps. The magnitude of reflection depends on the step structures. It is intuitively natural that reflection of the double QL step is stronger than that of the single QL step with the same type of step. It seems that there is no simple reason for the difference among step I, step II, and reverse slip structures.

Figure 5 shows amplitude distribution of wave functions obtained from the transmission calculation. The step structure is step I with single QL step height. The thickness of the slab is 5 QLs. Energy and parallel wave number are 0.2 eV and 0 Å^{-1}, respectively. Therefore, they are wave functions at the perfect transmission. The incident channel is the surface state localized on the upper or lower surface on the left side of the slab.

In the present study, step structures are made by inserting a slip into a flat slab. Since the left and right parts of the step structures divided by the slip plane are flat slabs, scattering occurs only on the slip plane. In principle, the scattering by the step structures can be expressed by recombination of the channels in the left and right slabs, where the channels include propagating and evanescent waves. However, it seems difficult to make a simple model to explain the calculated transmission property of the surface states from this picture.

Another picture is potential scattering of a massless Dirac electron. The wave function of Fig. 5 shows that the surface state on the terrace is localized within about one QL depth from the surface, and the transition region from the surface state of the lower terrace to that of the upper one has also the same order of width. It may be viewed as that current flows from the lower terrace to the upper one through a transition region. The scattering by steps is expressed by change in effective potential for the surface state in the transition region. This is similar to the model used in the discussion of transmission through atomic steps of the Si(111)$\sqrt{3} \times \sqrt{3}$-Ag surface.[23]

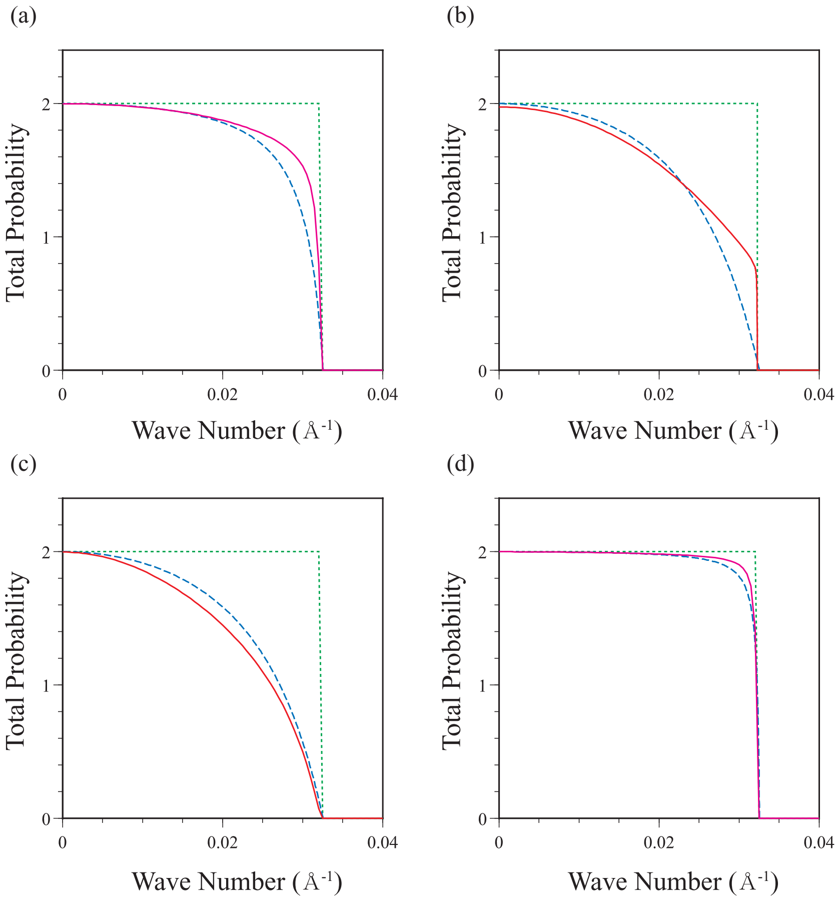

FIG. 4. (Color online) Total transmission probability through steps of a Bi_2Se_3 thin film as a function of the wave number parallel to the step line. Energy is 0.2 eV. (a) Step I with single QL height, (b) step I with double QL height, (c) step II with single QL height, and (d) step I with single QL height and reverse slip. Solid and dotted lines show transmission probability and the number of transmission channels, respectively. Broken lines show the transmission probability calculated by using a massless Dirac Hamiltonian.

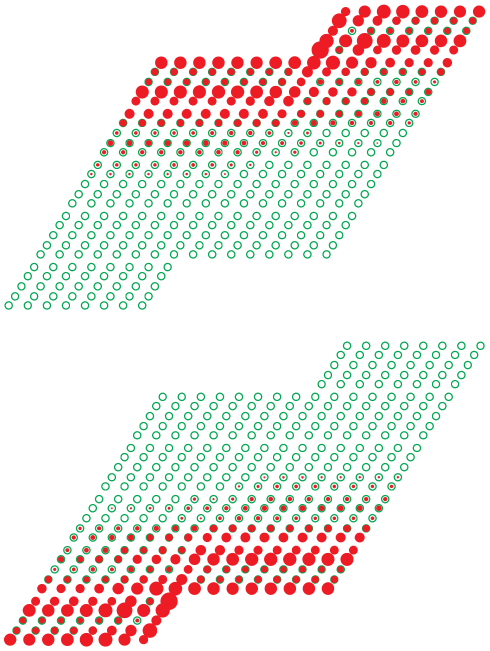

FIG. 5. (Color online) Amplitude distribution of wave functions near surface steps of Bi_2Se_3. The wave functions are calculated for the normal incidence. Open circles show the positions of atoms.

We consider the effective Hamiltonian for the surface states on terraces given by

$$\mathcal{H} = v(\hat{p}_x\sigma_y - \hat{p}_y\sigma_x), \tag{1}$$

where v is velocity, and σ_i is the i component of the Pauli matrix. $\hat{p}_x$ and $\hat{p}_y$ are the x and y components of the momentum operator, respectively. We add a potential with constant height V_0 in the transition region with width d. Transmission probability is analytically obtained as

$$T = \frac{1}{1 + \sin^2\phi\left(\frac{\sin\theta - \sin\theta'}{\cos\theta\cos\theta'}\right)^2}, \tag{2}$$

where θ is the angle of incidence and θ' is the angle of refraction in the transition region. ϕ is the phase of optical path given by $k'd$, where k' is the wave number in the transition region.

The broken lines in Fig. 4 show the transmission probability calculated using this effective model. v is 3.3 eV·Å, which is the value obtained from the tight-binding calculation shown in the Appendix. Energy is 0.1074 eV, which is chosen so that the maximum parallel wave number of propagating waves is the same as that of the tight-binding calculation. This corresponds to the energy of the tight-binding calculation in Fig. 4 because the energy of the Dirac point is about 0.1 eV in the tight-binding calculation shown in the Appendix.

Potential energy V_0 and width d are −0.129 eV and 9.84 Å for step I with single QL height, −0.203 eV and 9.84 × 2 Å for step I with double QL height, −0.279 eV and 15.24 Å for step II with single QL height, and

−0.046 eV and 9.84 Å for step I with a reverse slip. We adopt the minimum distance between the edges of the upper and lower terraces as the width of the transition region. The potential energy is determined by fitting to the numerical curves of tight-binding calculations. Though the curves of the effective model do not perfectly fit the numerical ones, the former qualitatively reproduce the latter. It may be concluded that the transmission through steps of the Bi_2Se_3 surface is understood in terms of a simple potential scattering model of the massless Dirac Hamiltonian.

There is a theoretical study reporting that surface states with anisotropic Dirac cones exist on the side surfaces of Bi_2Se_3,[22] where the transmission through a junction of a side surface sandwiched by two terraces is proposed. In this model, scattering occurs by the difference in velocity at junctions. However, this model seems not applicable to the present system because the side surfaces are too narrow in the atomic steps. The lower velocity of the side surface is 0.92 eV Å in Ref. 22. This corresponds to 58 Å in wavelength for 0.1 eV in energy. This length is much larger than the width of side surfaces of the atomic steps. Therefore it is not a clear picture in the present case that current flows through side surfaces. Actually this model does not explain the difference between the transmission properties of reverse slips shown in Figs. 4(a) and 4(d). This difference is explained by the difference in current distribution on atomic scales at steps. The difference in shape of step structures brings about different current distribution, which changes the potential effectively experienced by an electron in the transition region.

B. Bi_2Te_3

Figure 6 shows calculated transmission probability through a surface step of Bi_2Te_3. Transmission probability is calculated for the step I structure with single QL step height. The conditions of calculations are the same as the Bi_2Se_3 case shown in Fig. 3. The transmission properties are similar to the Bi_2Se_3 case. Finite reflection is seen for the surface states of 2 and 3 QL slabs, and almost perfect transmission is obtained for 4 and 5 QL slabs.

Figure 7 shows transmission probability as a function of the wave number parallel to the step line. Energy is 0.1 eV. The perfect transmission is obtained at normal incidence, and transmission probability decreases with increasing the parallel wave number. This behavior is common with the Bi_2Se_3 case. However, there is a distinct difference at large wave number. The transmission probability reaches the minimum, and increases with the wave number. The minimum value is zero except for the reverse slip step. Perfect reflection occurs at an angle of incidence. The existence of the perfect reflection is not restricted to special energy. The perfect reflection appears at an almost specific angle of incidence in the energy range of the bulk band gap.

The perfect reflection cannot be explained by the simple potential scattering of massless Dirac Hamiltonian used in the Bi_2Se_3 case. The perfect transmission can occur when the barrier width is a multiple of half wavelength in the barrier. However, the transmission probability is not zero even in the tunneling case. In order to clarify the origin of the perfect reflection, we show detailed calculations below.

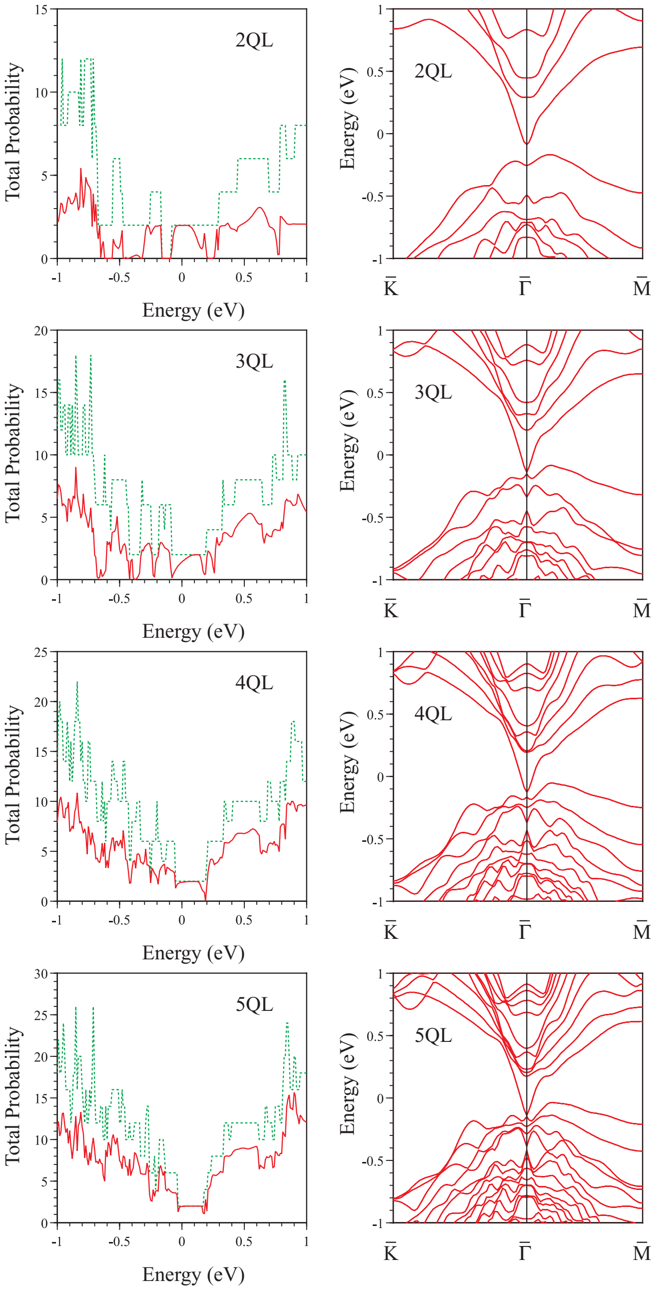

FIG. 6. (Color online) Total transmission probability through a 1 QL step of Bi_2Te_3 thin films as a function of energy. Probability is calculated for normal incidence to the step line. Solid and dotted lines show transmission probability and the number of transmission channels, respectively. The band structures of thin films without steps are also shown on the right side.

Figure 8 shows the amplitude of wave functions at the perfect reflection. The parallel wave number is 0.048 $Å^{-1}$, which is the value at perfect reflection in the spectrum of Fig. 7(a). The incident waves come from the left side. They are reflected by the steps and completely return to the left side. The distribution of wave functions is different between the two cases impinging on the steps from the upper and lower terraces. In the case impinging from the upper terrace, the wave is reflected by the side surface of the step, and the penetration into the lower terrace is weak. In the case impinging from the

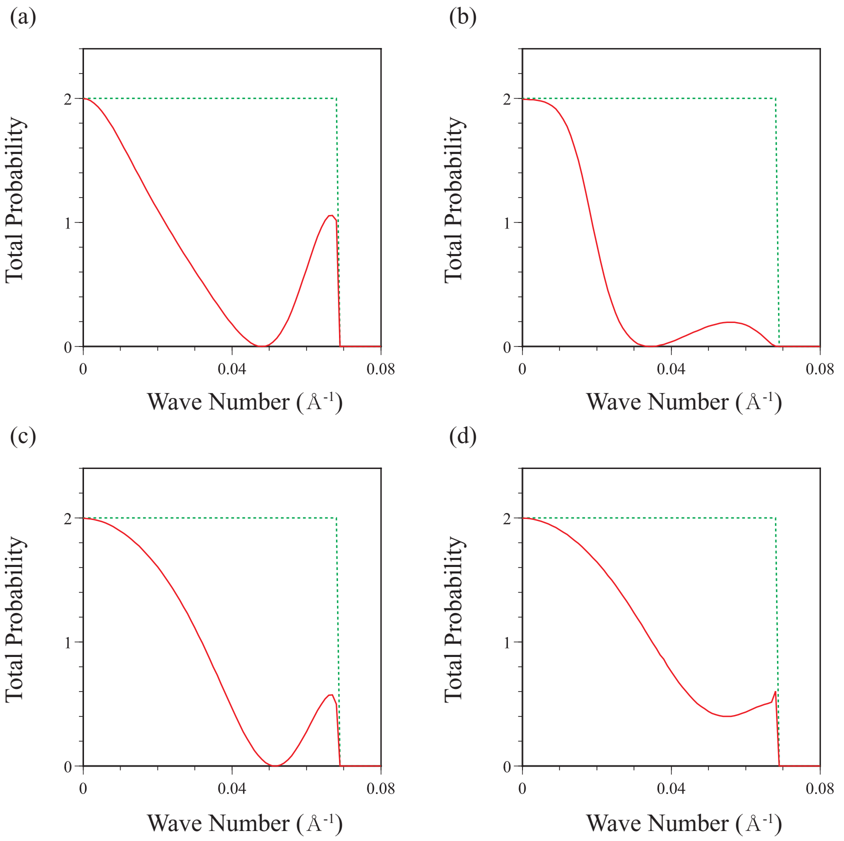

FIG. 7. (Color online) Total transmission probability through steps of a Bi_2Te_3 thin film as a function of the wave number parallel to the step line. Energy is 0.1 eV. (a) Step I with single QL height, (b) step I with double QL height, (c) step II with single QL height, and (d) step I with single QL height and reverse slip. Solid and dotted lines show transmission probability and the number of transmission channels, respectively.

lower terrace, the wave is reflected by the cliff of the bulk region underneath the upper terrace. The bulk region breaks the translational symmetry of the lower terrace and scatters the electrons in surface states. The wave function has appreciable amplitude in the bulk region underneath the upper terrace.

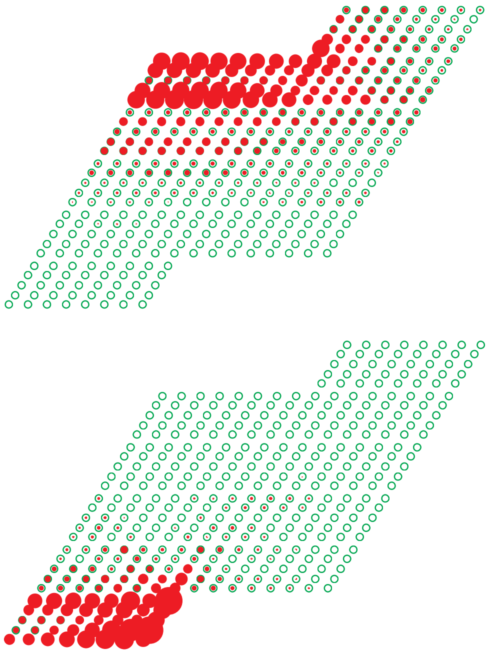

FIG. 8. (Color online) Amplitude distribution of wave functions near surface steps of Bi_2Te_3. The parallel wave number is 0.048 $Å^{-1}$. The transmission probability is zero at this wave number in the spectrum of Fig. 7(a). Open circles show the positions of atoms.

Since transmission probability is zero at perfect reflection, propagating waves in the wave functions are only the incident and reflected waves in the left side. All other waves are evanescent waves. In general, steps break the translational symmetry. The break of translational symmetry not only transforms an incident wave into transmitted and reflected waves but also causes coupling with evanescent waves. The perfect reflection means that the incident and reflected waves are coupled with only evanescent waves and disconnected from the transmitted wave. The transmitted wave is identical with the incident wave in the present system. But they are seamed together with shifts by step heights or slip lengths, and are decoupled by the reflected and evanescent waves at the perfect reflection. We have checked that the main components of evanescent waves in the wave functions at the perfect reflection are the left-decaying evanescent waves in the incident side in the case impinging from the upper terrace, and the right-decaying evanescent waves in the transmitted side in the case impinging from the lower terrace. In spite of the asymmetry in spatial distribution and components of the wave function, the transmission probability is zero at the same parallel wave number for the two cases with incident waves from the upper and lower terraces. This is due to the time-reversal symmetry.

The present perfect reflection has no relation to bound states localized at step edges. In order to show this, the band structure of a system where steps are periodically introduced in a slab is calculated. Figure 9 shows a band structure of a stepped Bi_2Te_3 slab. The stepped slab is made by periodically introducing

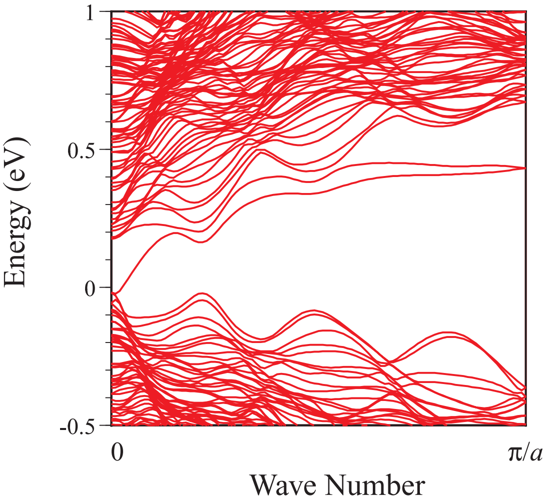

FIG. 9. (Color online) Band structure of a stepped Bi_2Te_3 thin film. Energy bands are shown as a function of the wave number parallel to the step line. a is the lattice constant.

steps of step I structure with 1 QL height into the surfaces of a flat slab. The terrace width is 10 times the unit cell of the flat surface. The thickness of the slab is 6 QLs. The state with linear dispersion near the zero wave number and around the energy region from 0 to 2 eV is the surface state on the flat Bi_2Te_3 surface.

The two bands with nearly flat dispersion around the energy of 0.4 eV and in the region of large wave number are states localized at step edges. We checked that these bands do not exist in a flat slab without steps. Figure 10 shows the wave function of the step-edge state. The terrace width is 15 times the unit cell of the flat surface. The thickness of the slab is 8 QLs. The wave number is $0.7\pi/a$ where a is the lattice constant in the direction along the step line. The state in the lower band is shown, but the difference in the wave functions of the lower and higher bands is small. The edge bands are doubly degenerated like the surface state on the flat surface. One and the other states are localized at the steps of the upper and lower surfaces of the slab, respectively. It has been verified that the edge states are the time-reversal states of the edge states with the opposite wave number and they are orthogonalized. However, since bulk bands exist in the energy range of the edge bands, electrons in the edge states are scattered to bulk states by nonmagnetic defects on step edges and perfect transmission does not occur. There is a report that the states localized at step edges of Bi_2Te_3 surfaces are observed experimentally.[25]

The step-edge states are not the origin of the perfect reflection in Fig. 7. The reasons are as follows. First, the edge-state bands are separated in energy from the Dirac cone of the surface state. They do not mix by elastic scattering. Second, the wave functions of the perfect reflection shown in Fig. 8 have asymmetry in the components of evanescent waves. The evanescent waves have main components in either upper or lower terrace. They accompany the incident and reflected propagating waves. In contrast, the wave functions of the step-edge states decay into both the upper and lower terraces. They exist without propagating waves. Third, we have calculated the band structure of a stepped slab for Bi_2Se_3, and checked the existence of step edge bands similar to those of Bi_2Te_3 shown in Fig. 9. However, the perfect reflection does not appear in the transmission spectra of Bi_2Se_3 as shown in Fig. 4. These results suggest that the origin of the perfect reflection is not the step-edge states but the difference in the structure of evanescent waves between Bi_2Se_3 and Bi_2Te_3 surfaces.

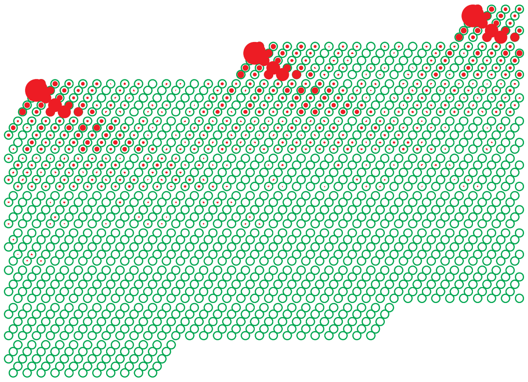

FIG. 10. (Color online) Squared amplitude of the wave function of the edge state localized at surface steps of Bi_2Te_3. Open circles show the position of atoms.

Finally in this section we show the difference in structures of evanescent waves between the Bi_2Se_3 and Bi_2Te_3 surfaces. In general wave function $\psi(\mathbf{r})$ of a periodic system satisfies

$$\psi(\mathbf{r}+\mathbf{a}) = e^{i\phi}\psi(\mathbf{r}), \tag{3}$$

where $\mathbf{a}$ is a lattice vector. When phase ϕ is a real number, it is a propagating Bloch state. When ϕ is a complex number, it is an evanescent state. Figure 11 shows decay constants of the generalized Bloch states as a function of the wave number parallel to the step line. The decay constants are given by the imaginary part of ϕ divided by a length. The lengths chosen for the Bi_2Se_3 and Bi_2Te_3 surfaces are 3.56 and 3.78 Å, respectively. They are the distances of neighboring atomic rows perpendicular to the step line. The thickness of the slab is 5 QLs. Energy is 0.2 and 0.1 eV for Bi_2Se_3 and Bi_2Te_3, respectively. The states with zero and nonzero decay constants are propagating and evanescent waves, respectively.

The structure of evanescent waves is qualitatively different between the Bi_2Se_3 and Bi_2Te_3 surfaces. The structure of Bi_2Se_3 is simple and the dependence on the wave number is weak. The structure of Bi_2Te_3 is complex and the dependence on the wave number is strong. This difference is explained by the difference in the bulk band structures of these materials. Figures 11(c) and 11(d) show band structures of the Bi_2Se_3 and Bi_2Te_3 thin films, respectively. The band structures show the dispersions parallel to $\bar{\Gamma}$-$\bar{\text{M}}$ for fixed wave vectors perpendicular to the $\bar{\Gamma}$-$\bar{\text{M}}$ line. Here, $\bar{\Gamma}$-$\bar{\text{M}}$ is perpendicular to the step line. Therefore, the two band structures displayed for each material show the contrast of dispersions at different wave numbers shown in Figs. 11(a) and 11(b). The band structures of the Bi_2Se_3 thin film do not show much differences except for the opening of the band gap of the Dirac cone at 0.1 eV. In contrast, those of the Bi_2Te_3 thin film are very different. In particular, the bulk bands above about 0.2 eV and below 0 eV

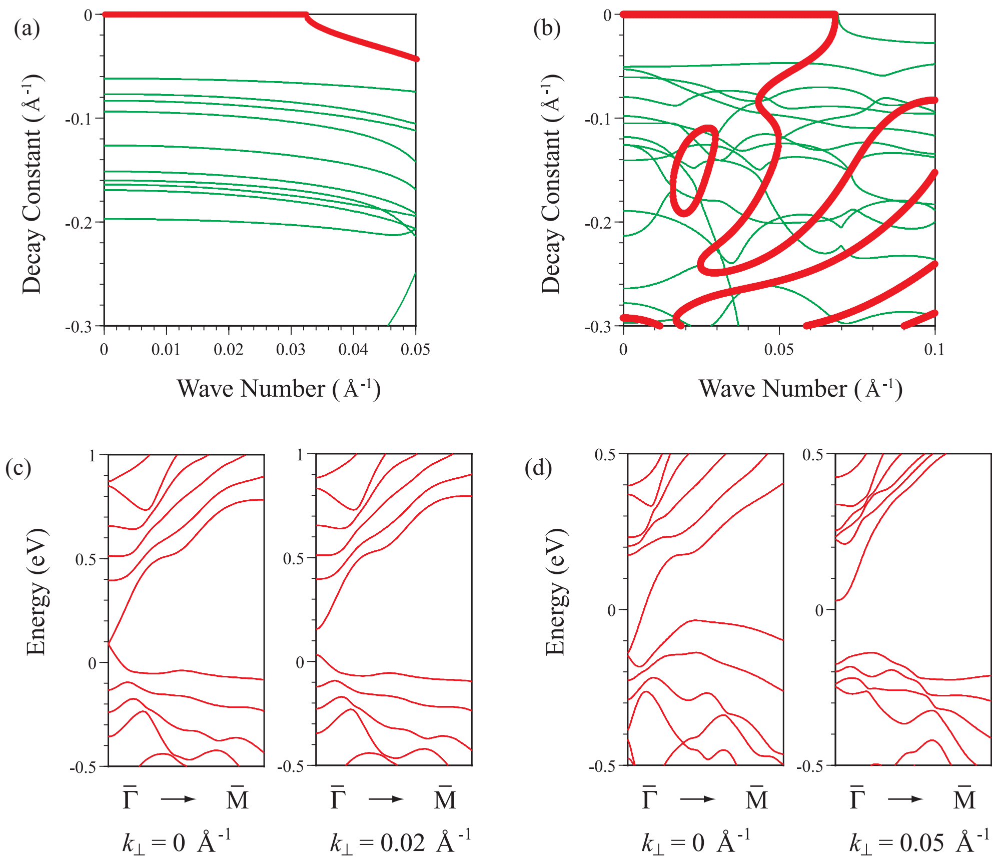

FIG. 11. (Color online) Decay constants of generalized Bloch states of Bi_2Se_3 (a) and Bi_2Te_3 (b) thin films as a function of the wave number parallel to the step line. The thickness of the thin films is 5 QLs. Energy is 0.2 and 0.1 eV for Bi_2Se_3 and Bi_2Te_3, respectively. The states shown by thick and thin lines are doubly and fourfold degenerated, respectively. Energy bands of the Bi_2Se_3 (c) and Bi_2Te_3 (d) thin films along lines parallel to $\bar{\Gamma}$-$\bar{M}$ for fixed wave vectors perpendicular to $\bar{\Gamma}$-$\bar{M}$. $\bar{\Gamma}$-$\bar{M}$ is perpendicular the step line. $k_\perp$ shows the norm of the perpendicular wave vectors and corresponds to the wave number in (a) and (b). The points at the left and right edges of bands correspond to $\bar{\Gamma}$ and the middle of $\bar{\Gamma}$-$\bar{M}$ line when they are projected along the perpendicular direction.

are qualitatively different. For example, the band crossings appearing in the dispersions parallel to $\bar{\Gamma}$-$\bar{M}$ are changed. This means that the energy order of bulk bands with the same character changes with varying the wave number in Fig. 11(b).

It is known that an evanescent state traces a line as a function of energy in the complex wave number space.[26,27] This so-called real line connects a local minimum of a conduction band and a local maximum of a valence band. When there are many evanescent states, each real line connects different conduction and valence bands. Therefore, it is natural that the structure of evanescent waves of the Bi_2Te_3 surface shows complex behavior as a function of the wave number shown in Fig. 11(b) when the bulk band structure largely changes as a function of the same wave number as shown in Fig. 11(d). A reason for the strong dependence on wave vectors of the bulk bands of Bi_2Te_3 may be seen in the bulk band structures of Fig. 14. The neighboring bands to the lowest conduction and highest valence bands of Bi_2Te_3 have closer proximity in energy to the latter bands than those of Bi_2Se_3. However, the complexity in the structure of evanescent waves is not directly related with the origin of the perfect reflection as shown below.

Another important difference in the structure of evanescent waves is seen in the way of linking of the evanescent waves with the propagating ones of the Dirac cones. The thick and thin lines show doubly and fourfold degenerated states, respectively. The propagating waves with zero decay constant are surface states with the Dirac cones, and they are doubly degenerated. One is localized at the upper surface of the slab and the other is at the lower one. In the case of the Bi_2Se_3 surface they simply change into evanescent waves at 0.032 Å which is the border wave number of the Dirac cone. There is no other doubly degenerated state. In the case of the Bi_2Te_3 surface the propagating states coexist with doubly degenerated evanescent ones inside the Dirac cone less than 0.068 Å, and they touch near the border wave number of the Dirac cone. This result suggests that the coexistence of the propagating states with the evanescent states that are linked to the propagating ones is important for the existence of perfect reflection in the Bi_2Te_3 case.

With respect to the differences between Bi_2Se_3 and Bi_2Te_3, it is well known that hexagonal warping of the Dirac cone is strong in the Bi_2Te_3 surface.[19] The hexagonal-warping effect is usually used for explaining the deformation of the shape of Dirac cones. However, it gives an effect having another aspect in transport properties. The circularly symmetrical Dirac cone given by the Hamiltonian in Eq. (1) reproduces the structure of doubly degenerate states of Bi_2Se_3 in Fig. 11. But, it does not explain the coexistence of the propagating and doubly degenerated evanescent waves of $\mathrm{Bi_2Te_3}$. Since the hexagonal-warping term is a higher order term of momentum, it produces a richer structure in energy-momentum space. This has a large effect on transport properties. In order to show this we present a calculation of transmission with the hexagonal-warping term in the next section.

IV. TRANSMISSION OF A MASSLESS DIRAC PARTICLE WITH HEXAGONAL WARPING

The effective Hamiltonian of surface states with the hexagonal-warping term is given by

$$\mathcal{H} = v(\hat{p}_x\sigma_y - \hat{p}_y\sigma_x) + \lambda\left(\frac{\hat{p}_+^3 + \hat{p}_-^3}{2}\right)\sigma_z, \tag{4}$$

where λ is the parameter of hexagonal warping.[19] $\hat{p}_\pm$ are given by $\hat{p}_x \pm i\hat{p}_y$, respectively. The x axis is parallel to the $\bar{\Gamma}$-$\bar{\mathrm{K}}$ line. This gives the energy-momentum relation for plane-wave solutions as

$$E^2 = v^2p^2 + \lambda^2\left(p_x^3 - 3p_xp_y^2\right)^2. \tag{5}$$

When the hexagonal-warping term is absent, this is a quadratic equation of both p_x and p_y. Either propagating or evanescent waves exist in this case. However, when the hexagonal-warping term is present, this is an equation of the sixth and fourth degree for p_x and p_y, respectively. The step line of the steps studied in this paper is parallel to x axis. Therefore, p_x is conserved across the steps and is a real number. Since the equation is a quartic equation of p_y, there are four solutions for fixed E and p_x. Equation (5) expresses the single Dirac cone of the $\mathrm{Bi_2Te_3}$ surface. Therefore, the number of propagating waves is either two or four. When the number of propagating waves is two, other waves are evanescent waves. The hexagonal-warping term brings about the coexistence of propagating and evanescent waves.

We consider transmission through a potential barrier. We add potential $V(y)$ to the Hamiltonian in Eq. (4), where $V(y)$ is given by

$$V(y) = \begin{cases} 0 & (y < 0, y > d), \\ V_0 I & (0 < y < d). \end{cases} \tag{6}$$

d and V_0 are width and height of the barrier. I is the 2×2 identity matrix.

We consider, for example, the case that the numbers of propagating and evanescent waves are two in the whole system. In this case the wave function is set as

$$\Psi = e^{ik_xx}(e^{ik_yy}\mathbf{u}_{p+} + re^{-ik_yy}\mathbf{u}_{p-} + Ae^{\lambda_-y}\mathbf{u}_{e-}), \tag{7}$$

in the region of $y < 0$,

$$\begin{aligned}\Psi = e^{ik_xx}(&Be^{ik'_yy}\mathbf{u}'_{p+} + Ce^{-ik'_yy}\mathbf{u}'_{p-} \\ &+ De^{\lambda'_+y}\mathbf{u}'_{e+} + Ee^{\lambda'_-y}\mathbf{u}'_{e-}),\end{aligned} \tag{8}$$

in the region of $0 < y < d$, and

$$\Psi = e^{ik_xx}(te^{ik_yy}\mathbf{u}_{p+} + Fe^{\lambda_+y}\mathbf{u}_{e+}), \tag{9}$$

in the region of $y > d$. In the above, t and r are transmission and reflection coefficients. A, B, C, D, E, and F are coefficients. $\hbar k_y$ and $-\hbar k_y$ are real solutions of Eq. (5), where $\hbar k_y$ is the state with positive group velocity. $\hbar\lambda_+$ and $\hbar\lambda_-$ are complex solutions of Eq. (5) multiplied by the imaginary unit. The real parts of λ_+ and λ_- are negative and positive, respectively. $\mathbf{u}_{p+}$, $\mathbf{u}_{p-}$, $\mathbf{u}_{e+}$, and $\mathbf{u}_{e-}$ are corresponding eigenvectors of the Hamiltonian in Eq. (4), where subscripts p and e mean propagating and evanescent waves, respectively. The quantities with primes are similarly defined in the region of $0 < y < d$. When the number of propagating waves is four, there are two incident channels and the wave function is similarly set for each incident channel.

Since the Schrödinger equation given by the Hamiltonian in Eq. (4) is a second-order differential equation of y, we require two conditions at a boundary. We simply assume the continuities of wave function Ψ and velocity $\hat{v}_y\Psi$ at $y = 0$ and $y = d$,[28,29] where $\hat{v}_y$ is the velocity operator given by

$$\hat{v}_y = \frac{\partial\mathcal{H}}{\partial\hat{p}_y}. \tag{10}$$

These two conditions guarantee the conservation of y component of current across a boundary.

Figure 12(a) shows transmission probability as a function of k_x. We use 2.55 eV·Å and 250 eV·Å^3 for parameters v and λ, respectively.[19] Energy E, barrier width d, and potential height V_0 are 0.2 eV, 17 Å, and 0.4 eV, respectively. The energy is determined so that the maximum wave number of the Dirac cone agrees with that in Fig. 7. It roughly corresponds to the energy of 0.1 eV in Fig. 7 because the Dirac point is −0.14 eV in the tight-binding calculation shown in the Appendix. The barrier width and potential height are chosen to approximately reproduce the spectrum in Fig. 7(a). The value of the barrier width is reasonable because it is slightly larger than 12 Å which is the width of the side surface of step I with single QL height. The spectrum without the hexagonal-warping term is also shown for comparison. The spectrum with the hexagonal-warping term in Fig 12(a) reproduces the spectrum of the tight-binding calculation in Fig. 7(a). Perfect reflection appears at $k_x = 0.048$ Å^{-1}. The spectrum abruptly drops to zero at about $k_x = 0.07$ Å^{-1}. This originates from the singular shape of the hexagonally warped Dirac cone. In order to understand this, the constant energy line of the Dirac cone at 0.2 eV is shown in the inset of Fig. 12(a). The transmission probability without the hexagonal-warping term monotonically decreases with the wave number.

Figure 12(b) shows the wave function at the perfect reflection. The region of the potential barrier is $0 < y < 17$ Å. The wave function exponentially decays in the region of $y > 17$ Å. A standing wave is formed in the region of $y < 0$ Å. The height of the first peak of the standing wave is higher than others because the evanescent wave does not completely decay at the first peak. The phase shift is different between the up and down components of spin. This gives rise to two results. One is that the two regions where net spin is up and down alternate, making a periodical spin structure in standing waves like an anti-ferromagnet. Second is that the total standing wave has no node. The spin-dependent phase shift is not specific to the perfect reflection. It appears at any parallel wave number. This means that careful consideration may be necessary to analyze data of standing waves measured by spin-independent STS.

Figure 13 shows decay constants as a function of k_x. The decay constants are given by the imaginary part of $p_y/\hbar$ where p_y is a solution of Eq. (5). This structure of evanescent states

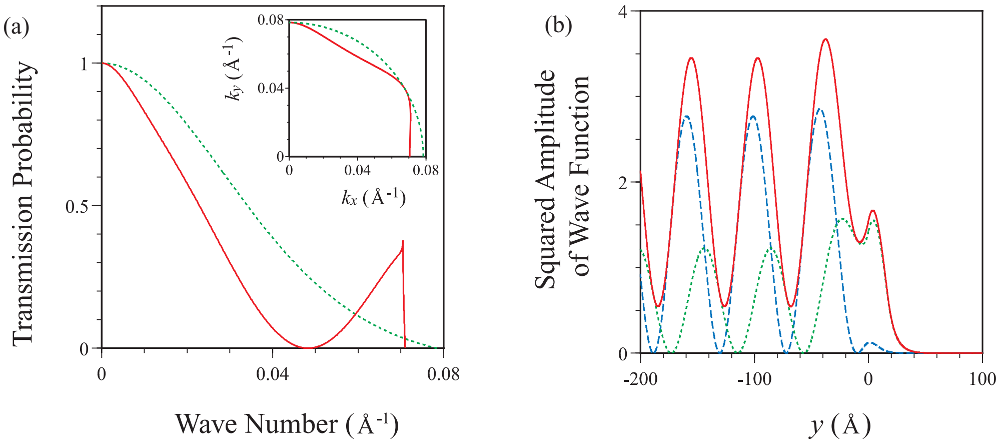

FIG. 12. (Color online) (a) Transmission probability as a function of wave number k_x. Solid and dotted lines show the probability with and without the hexagonal-warping term, respectively. The inset shows constant-energy lines of the Dirac cone at energy of 0.2 eV. Solid and dotted lines show the Dirac cones with and without the hexagonal-warping term, respectively. (b) Wave function at $k_x = 0.0483$ Å^{-1}. Solid line shows total squared amplitude of the wave function. Dotted and broken lines show the components with up and down spins, respectively.

qualitatively explains the structure of doubly degenerated states of the Bi_2Te_3 surface in Fig. 11(b). The propagating state exists in the region of $k_x < 0.07$ Å^{-1}. The evanescent state in this region roughly corresponds to the doubly degenerated evanescent state with the longest decay length in Fig. 11(b). The propagating and evanescent states meet at $k_x = 0.07$ Å^{-1} and change into a degenerated evanescent state in the region of $k_x > 0.07$ Å^{-1}. They correspond to the fourfold degenerated states in Fig. 11(b). Since the effective Hamiltonian of Eq. (4) has only four channels, it does not explain all the evanescent states in Fig. 11(b). However, the effective Hamiltonian can explain the existence of perfect reflection and reproduce qualitatively the transmission spectrum. It describes the essence of the transport properties.

The perfect reflection in the present system is essentially similar to that expected in bilayer graphene.[20] The effective Hamiltonian of a bilayer graphene is a quadratic equation of momentum with a two-component pseudospinor. This equation also gives rise to the coexistence of propagating and evanescent waves. The situation is simpler in bilayer graphene. The pseudospinor is decoupled into propagating and evanescent components for normal incidence at a junction. It is clear that propagating waves couple only with evanescent waves and vise versa at an *np* junction, and perfect reflection occurs.

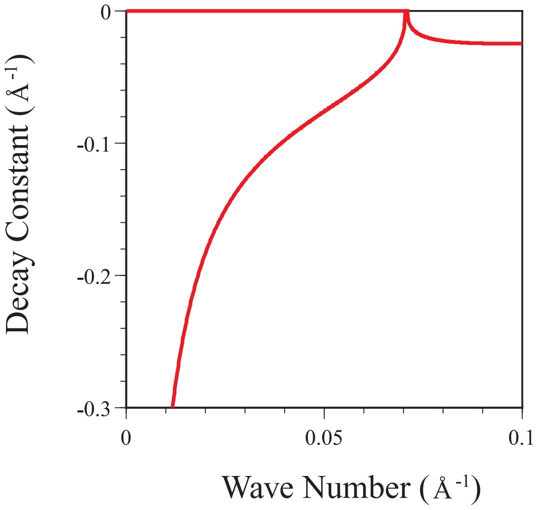

FIG. 13. (Color online) Decay constants of the massless Dirac Hamiltonian with the hexagonal-warping term. The decay constants are shown as a function of wave number k_x for energy $E = 0.2$ eV.

The perfect reflection induced by the hexagonal-warping term is complicated. It occurs at an oblique angle of incidence. The spinors of propagating and evanescent waves are not orthogonalized. Nevertheless, it has a similarity with the bilayer graphene. It occurs at *np* and *npn* junctions. The setting of energy E and barrier height V_0 in Fig. 12 forms an *npn* junction. We checked that perfect reflection is not found in the setting of *nnn* junctions, and it appears in an *np* junction in the present system. Perfect reflection does not appear in the reverse-slip case shown in Fig. 7(d). This result is explained by that the effective potential forms an *nnn* junction in the reverse-slip case.

Perfect reflection appears also in a system with a δ-function potential instead of the potential barrier with a finite width. In this case a discontinuity in the first derivative of the wave function is introduced at the boundary. The perfect reflection appears in the δ-function potential with a positive sign for positive energy E, which corresponds to an *npn* junction with a zero width. The δ-function potential with constant strength does not reproduce the perfect transmission at normal incident. This is due to the fact that the quadratic term of p_y in the hexagonal-warping term vanishes at $p_x = 0$, which requires infinitely large discontinuity of the first derivative. Therefore, the potential strength should depend on wave number and approach zero with the approach of p_x to zero. Then the perfect transmission recovers at normal incidence.

It is reported that the Dirac cone of the Bi_2Se_3 surface is not perfectly circular but hexagonally warped.[30] But the degree of warping is smaller than the Bi_2Te_3 surface. We calculate the transmission probability for the Bi_2Se_3 surface with taking account of the weak hexagonal-warping effect.

We use 3.55 eV·Å and 128 eV·Å^3 for parameters v and λ of the Bi_2Se_3 surface shown in Ref. 30, respectively. We choose the same values for energy E, barrier width d, and potential V_0 as those in the calculation of the Bi_2Te_3 surface shown in Fig. 12. The calculated transmission probability shows monotonic decrease as a function of k_x, and no perfect reflection is found. These results are common with the tight-binding calculations in Fig 4, and the hexagonal-warping effect is not essentially important in the transmission properties of the Bi_2Se_3 surface. The absence of perfect reflection is explained as follows. The parallel wave number, at which perfect reflection appears, depends on the magnitude of hexagonal-warping parameter λ. With decreasing λ, the wave number of perfect reflection shifts to the larger wave number side. The wave number at which the conditions for perfect reflection are satisfied is much shifted in the case of the Bi_2Se_3 surface due to the weak hexagonal warping, and it overshoots the boundary of the Dirac cone. Therefore, perfect reflection does not appear in the transmission spectra. When energy E is raised to 0.3 eV in order to strengthen the hexagonal-warping effect, perfect reflection appears even in the case of the Bi_2Se_3 surface. However, since bulk bands coexist with the surface-state bands in this energy region, the perfect reflection would not appear in a realistic system of Bi_2Se_3 due to the scattering to bulk states.

An origin of the difference in the strength of hexagonal warping between the Bi_2Se_3 and Bi_2Te_3 surface may be the orbital character of the surface states. The main component of the surface state of the Bi_2Se_3 surface is p_z orbital, where z axis is perpendicular to the surface. The surface state of the Bi_2Te_3 surface has a large amount of p_x and p_y components. The typical percentages of p_z and p_x plus p_y components are 67% and 29% for the surface state of Bi_2Se_3 at energy about 0.2 eV in the present tight-binding calculation. Those for Bi_2Te_3 are 35% and 62% at about 0.1 eV.

V. CONCLUSION

We presented electron transmission across surface steps of Bi_2Se_3 and Bi_2Te_3 calculated by a tight-binding method. We studied mainly the transmission of the surface states in the bulk band gaps of these surfaces. In both cases the almost perfect transmission appears from 4 QL slabs. The feature of the transmission spectra as a function of the incident angle with respect to step lines is different between these cases. The transmission probability of Bi_2Se_3 monotonically decreases with increasing the incident angle. The magnitude of decrease depends on the atomic structure of steps. These spectra are reproduced by a potential scattering model of the massless Dirac Hamiltonian.

The transmission spectra of Bi_2Te_3 do not monotonically decrease with the incident angle, but perfect reflection exists at an oblique angle. The perfect reflection is not explained by only the massless Dirac Hamiltonian. The hexagonal-warping term is necessary for its existence. The massless Dirac Hamiltonian with the hexagonal-warping term contains not only propagating waves but also evanescent waves. This allows propagating waves to couple with only an evanescent wave at a junction, and causes perfect reflection. This mechanism of perfect reflection is similar to that of the bilayer graphene. We found different phase shifts for up and down spins in the reflection by steps, which forms stripe structures of spin density in standing waves.

The standing waves observed on the Bi_2Te_3 surface are explained by the hexagonal-warping effect.[6,7,19] The shape of the Dirac cone of the Bi_2Te_3 surface gradually changes from circle to concaved hexagram as energy distance increases from the Dirac point.[12] The concaved hexagram has a nesting structure, which enhances the density of states of the standing waves with special wave vectors. The observation of standing waves in experiments is usually explained by the warped shape of the Dirac cone.

The perfect reflection found in this paper adds a new factor to the formation of standing waves. The parallel wave vector at the perfect reflection is close to the nesting positions of the hexagonally warped Dirac cone. Therefore the standing wave should be enhanced by the transmission factor also. The perfect reflection exists even when energy is not far from the Dirac point, where the shape of the Dirac cone is convex and has no nesting structure. This may explain two experimental facts. One is that the standing waves by surface steps are observed even at energy lower than the energy region, in which the standing waves around point defects are observed.[6] Second is that standing waves by rough steps are not observed below the energy region of the concaved hexagram.[7] The perfect reflection exists for atomically straight steps in the present paper.

ACKNOWLEDGMENTS

Numerical calculations were performed by using supercomputers at the Institute of Solid State Physics and Information Technology Center, the University of Tokyo. This work was supported by Grants-in-Aid for Scientific Research from the Japan Society for the Promotion of Science.

APPENDIX: DETAILS OF TIGHT-BINDING CALCULATIONS

This appendix describes details of the tight-binding calculation. We use a tight-binding method with s and p orbitals. We take account of the transfers between atoms in the neighboring layers, the same layers, and the second-neighbor layers. The spin-orbital interaction is included in the intra-atomic matrix elements.[21] The tight-binding parameters are determined by fitting to bulk band structures obtained by a density-functional method. We use the WIEN2k package for the density-functional calculations.[31] The wave function is solved by the full-potential linearized augmented plane wave method. $8 \times 8 \times 8$ k points in the Brillouin zone are used. The generalized gradient approximation by Perdew, Burke, and Ernzerhof[32] is used for the exchange-correlation potential. We use the crystal structures in Ref. 33.

We fit with high weights a few bands near the Fermi energy in both the valence and conduction bands. In particular we determine the parameters to reproduce accurately the dispersions of the highest valence and lowest conduction bands on the Γ-Z line and the half part of the Z-F line near Z point in the bulk Brillouin zone because the top of valence bands and the bottom of conduction bands are located near these lines.

TABLE I. Tight-binding parameters of Bi_2Se_3. Energy is shown in eV. Lengths show the distances between atoms.

On Site	Bi	Se(1)	Se(2)
ε_s	−10.7629	−10.9210	−13.1410
ε_p	0.2607	−1.5097	−1.1893
Δ_{SO}	2.0666	0.3197	0.3632
Nearest-Neighbor	Bi-Se(1)	Bi-Se(2)	Se(1)-Se(1)
Layer	(2.926 Å)	(3.030 Å)	(3.354 Å)
$ss\sigma$	−0.6770	−0.2410	−0.3326
$sp\sigma$	2.0774	−0.2012	−0.0150
$ps\sigma$	−0.4792	−0.0193	0.0150
$pp\sigma$	2.0595	2.0325	0.9449
$pp\pi$	−0.4432	−0.5320	−0.1050
	Bi-Bi	Se(1)-Se(1)	Se(2)-Se(2)
Intralayer	(4.114 Å)	(4.114 Å)	(4.114 Å)
$ss\sigma$	0.2212	−0.0640	−0.0878
$sp\sigma$	−0.3067	0.2833	−0.2660
$pp\sigma$	0.3203	0.3047	−0.1486
$pp\pi$	−0.0510	−0.0035	−0.0590
Second-Neighbor	Se(1)-Se(2)	Bi-Bi	Bi-Se(1)
Layer	(4.305 Å)	(4.449 Å)	(4.719 Å)
$ss\sigma$	0.0229	−0.0567	0.0333
$sp\sigma$	−0.0318	−0.2147	−0.0047
$ps\sigma$	−0.0778	0.2147	0.2503
$pp\sigma$	−0.0852	0.1227	−0.1101
$pp\pi$	0.0120	−0.0108	0.1015

TABLE II. Tight-binding parameters of Bi_2Te_3. Energy is shown in eV. Lengths show the distances between atoms.

On Site	Bi	Te(1)	Te(2)
ε_s	−9.9967	−10.4977	−10.8744
ε_p	−0.3774	−1.5684	−1.0189
Δ_{SO}	1.9260	0.7292	0.7820
Nearest-Neighbor	Bi-Te(1)	Bi-Te(2)	Te(1)-Te(1)
Layer	(3.108 Å)	(3.218 Å)	(3.562 Å)
$ss\sigma$	−0.5815	−0.3734	−0.2926
$sp\sigma$	1.9027	−0.5901	−0.1142
$ps\sigma$	−0.6636	−0.6020	0.1142
$pp\sigma$	1.9956	1.9354	1.1364
$pp\pi$	−0.4868	−0.5084	−0.1792
	Bi-Bi	Te(1)-Te(1)	Te(2)-Te(2)
Intralayer	(4.369 Å)	(4.369 Å)	(4.369 Å)
$ss\sigma$	−0.0132	0.0484	0.0771
$sp\sigma$	−0.3312	0.0961	−0.0256
$pp\sigma$	0.1986	0.3243	0.0286
$pp\pi$	−0.0299	0.0399	−0.0927
Second-Neighbor	Te(1)-Te(2)	Bi-Bi	Bi-Te(1)
Layer	(4.571 Å)	(4.725 Å)	(5.011 Å)
$ss\sigma$	0.0807	−0.0912	0.0496
$sp\sigma$	−0.0659	−0.0592	−0.0369
$ps\sigma$	−0.0572	0.0592	−0.0184
$pp\sigma$	−0.0390	−0.0614	−0.1993
$pp\pi$	0.0571	0.0584	0.0828

Here, the wave vectors are given by $\Gamma(0,0,0)$, $Z(\frac{1}{2},\frac{1}{2},\frac{1}{2})$, and $F(\frac{1}{2},\frac{1}{2},0)$ in the units of reciprocal lattice vectors of the trigonal unit cell. The average of difference between the tight-binding and density-functional bands is about 0.005 eV on these lines. We tried fitting without the transfers between second-neighbor layers or s orbitals, but we did not find parameters which reproduce the bands near the Fermi energy with satisfactory precision.

Tables I and II show the determined tight-binding parameters. The origin of energy is the top of the bulk valence bands. Δ_{SO} is the energy splitting of p orbitals of an atom. One third of Δ_{SO} is the matrix element value of spin-orbital interaction. Se(1) and Te(1) denote the outer atoms of a QL layer, and Se(2) and Te(2) are the center atoms.

Figure 14 shows bulk band structures calculated using these parameters. The L point is given by $L(0,0,\frac{1}{2})$. The

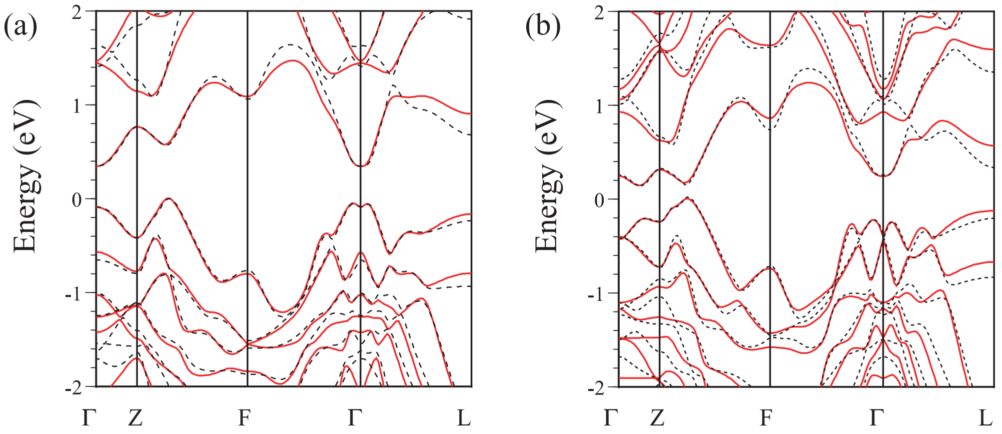

FIG. 14. (Color online) Bulk band structures of Bi_2Se_3 (a) and Bi_2Te_3 (b). Solid and dotted lines show the band structures obtained by the tight-binding and density-functional methods, respectively.

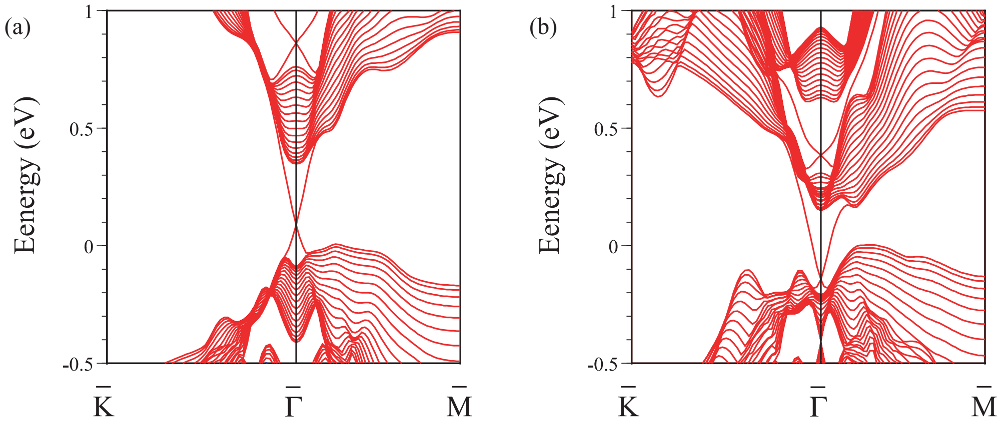

FIG. 15. (Color online) Band structures of Bi_2Se_3 (a) and Bi_2Te_3 (b) (111) thin films calculated by the tight-binding method. The thickness of the thin films is 20 QLs.

tight-binding band structures reproduce those obtained by the density-functional method near the Fermi energy, and they are similar to other density-functional calculations.[9,11]

Figure 15 shows band structures of (111) slabs calculated by the tight-binding method. These surface band structures are essentially similar to those of other calculations[9–12] and ARPES experiments.[10,12] The group velocity of the Dirac cones is 3.3 eV·Å (5.0×10^5 m/s) for Bi_2Se_3, and 2.9 eV·Å (4.4×10^5 m/s) along $\bar{\Gamma}$-$\bar{K}$ and 2.8 eV·Å (4.3×10^5 m/s) along $\bar{\Gamma}$-$\bar{M}$ for Bi_2Te_3. They correspond to the experimental values of 5×10^5 m/s for Bi_2Se_3,[10] and 4.05×10^5 m/s along $\bar{\Gamma}$-$\bar{K}$ and 3.87×10^5 m/s along $\bar{\Gamma}$-$\bar{M}$ for Bi_2Te_3.[12]

The Dirac point in the Bi_2Se_3 surface is located at 0.08 eV above the top of bulk valence bands. It is located slightly below the top of bulk valence bands in other calculations[11,34,35] except for one in Ref. 9. An STS experiment shows scattering of surface states to bulk states at the Dirac point, indicating that the Dirac point is below the top of the bulk valence bands.[36] On the other hand, a quasiparticle calculation shows that the Dirac point is 0.07 eV above the top of the bulk valence bands.[37]

We performed density-functional calculations using other experimental lattice parameters[38] and different exchange-correlation potentials.[39] But the bulk band structures are essentially similar, and the tight-binding parameters fitted to these bands give the position of the Dirac point above the top of the bulk valence bands. It is possible to move the position of the Dirac point by shifting the on-site energy of atomic orbitals in the surface QL because it is natural that the potential of surface atoms may be different from that of inner atoms. However, we do not do this tuning because we discuss the transmission of surface states in the bulk band gap above the Dirac point in this paper. The position of the Dirac point is not crucial.

Tables III and IV show band gaps of Dirac cones of Bi_2Se_3 and Bi_2Te_3 (111) thin films. The results calculated by the density-functional method using the WIEN2K package are also shown. It is theoretically predicted that the band gap in Bi_2Se_3 thin films oscillates as a function of the film thickness.[40–42] The present tight-binding calculation shows monotonic decrease of the band gap with increase of the film thickness. Our density-functional calculation also shows monotonic decrease. An experiment provides data suggesting the oscillating behavior,[43] but another experiment shows monotonic decrease of the band gap.[44] The quasiparticle calculation shows monotonic decrease of the band gap.[37] In this paper we discuss the transmission properties through surface steps, where the interaction between the surface states localized on the upper and lower surfaces of thin films can be neglected. Therefore the band gap in thin films with finite thickness is not essentially important.

TABLE III. Band gaps of Bi_2Se_3 (111) thin films. Energy is shown in eV. TB, DF, and EXP represent tight binding, density function, and experiment, respectively.

Thickness (QL)	TB	DF (Present)	EXP[44]	EXP[43]	DF[41]
1	0.837	0.841			0.710
2	0.179	0.205	0.252	0.28	0.098
3	0.043	0.075	0.138	0.34	0.004
4	0.008	0.028	0.070		0.012
5	0.000	0.008	0.041		0.004

TABLE IV. Band gaps of Bi_2Te_3 (111) thin films. Energy is shown in eV. TB and DF represent tight binding and density function, respectively.

Thickness (QL)	TB	DF (Present)	DF[45]	DF[41]
1	0.555	0.439	0.4338	0.391
2	0.168	0.103	0.1319	0.148
3	0.010	0.029	0.0261	0.036
4	0.037	0.033	0.0070	0.005
5	0.007	0.004	0.0090	

[1] M. Z. Hasan and C. L. Kane, Rev. Mod. Phys. **82**, 3045 (2010).
[2] X.-L. Qi and S.-C. Zhang, Rev. Mod. Phys. **83**, 1057 (2011).
[3] M. König, H. Buhmann, L. W. Molenkamp, T. Hughes, C.-X. Liu, X.-L. Qi, and S.-C. Zhang, J. Phys. Soc. Jpn. **77**, 031007 (2008).
[4] X.-L. Qi and S.-C. Zhang, Phys. Today **63**, 33 (2010).
[5] P. Roushan, J. Seo, C. V. Parker, Y. S. Hor, D. Hsieh, D. Qian, A. Richardella, M. Z. Hasan, R. J. Cava, and A. Yazdani, Nature (London) **460**, 1106 (2009).
[6] T. Zhang, P. Cheng, X. Chen, J.-F. Jia, X. Ma, K. He, L. Wang, H. Zhang, X. Dai, Z. Fang *et al.*, Phys. Rev. Lett. **103**, 266803 (2009).
[7] Z. Alpichshev, J. G. Analytis, J.-H. Chu, I. R. Fisher, Y. L. Chen, Z. X. Shen, A. Fang, and A. Kapitulnik, Phys. Rev. Lett. **104**, 016401 (2010).
[8] J. Seo, P. Roushan, H. Beidenkopf, Y. S. Hor, R. J. Cava, and A. Yazdani, Nature (London) **466**, 343 (2010).
[9] H. Zhang, C.-X. Liu, X.-L. Qi, X. Dai, Z. Fang, and S.-C. Zhang, Nature Phys. **5**, 438 (2009).
[10] Y. Xia, D. Qian, D. Hsieh, L. Wray, A. Pal, H. Lin, A. Bansil, D. Grauer, Y. S. Hor, R. J. Cava *et al.*, Nature Phys. **5**, 398 (2009).
[11] W. Zhang, R. Yu, H.-J. Zhang, X. Dai, and Z. Fang, New J. Phys. **12**, 065013 (2010).
[12] Y. L. Chen, J. G. Analytis, J.-H. Chu, Z. K. Liu, S.-K. Mo, X. L. Qi, H. J. Zhang, D. H. Lu, X. Dai, Z. Fang *et al.*, Science **325**, 178 (2009).
[13] J. Wang, W. Li, P. Cheng, C. Song, T. Zhang, P. Deng, X. Chen, X. Ma, K. He, J.-F. Jia *et al.*, e-print arXiv:1105.1957.
[14] X. Zhou, C. Fang, W.-F. Tsai, and J. Hu, Phys. Rev. B **80**, 245317 (2009).
[15] W.-C. Lee, C. Wu, D. P. Arovas, and S.-C. Zhang, Phys. Rev. B **80**, 245439 (2009).
[16] H.-M. Guo and M. Franz, Phys. Rev. B **81**, 041102(R) (2010).
[17] R. R. Biswas and A. V. Balatsky, Phys. Rev. B **83**, 075439 (2011).
[18] Q.-H. Wang, D. Wang, and F.-C. Zhang, Phys. Rev. B **81**, 035104 (2010).
[19] L. Fu, Phys. Rev. Lett. **103**, 266801 (2009).
[20] M. I. Katsnelson, K. S. Novoselov, and A. K. Geim, Nature Phys. **2**, 620 (2006).
[21] W. A. Harrison, *Elementary Electronic Structure* (World Scientific Publishing, Singapore, 1999), Chap. 5-3 G.
[22] C.-Y. Moon, J. Han, H. Lee, and H.-J. Choi, Phys. Rev. B **84**, 195425 (2011).
[23] K. Kobayashi, Surf. Sci. **583**, 16 (2005).
[24] H. H. B. Sørensen, P. C. Hansen, D. E. Petersen, S. Skelboe, and K. Stokbro, Phys. Rev. B **79**, 205322 (2009).
[25] Z. Alpichshev, J. G. Analytis, J.-H. Chu, I. R. Fisher, and A. Kapitulnik, Phys. Rev. B **84**, 041104(R) (2011).
[26] V. Heine, Proc. Phys. Soc. London **81**, 300 (1963).
[27] V. Heine, Surf. Sci. **2**, 1 (1964).
[28] T. Yokoyama, Y. Tanaka, and N. Nagaosa, Phys. Rev. Lett. **102**, 166801 (2009).
[29] E. Zhao, C. Zhang, and M. Lababidi, Phys. Rev. B **82**, 205331 (2010).
[30] K. Kuroda, M. Arita, K. Miyamoto, M. Ye, J. Jiang, A. Kimura, E. E. Krasovskii, E. Chulkov, H. Iwasawa, T. Okuda *et al.*, Phys. Rev. Lett. **105**, 076802 (2010).
[31] P. Blaha, K. Schwarz, G. K. H. Madsen, D. Kvasnicka, and J. Luitz, WIEN2K, *An Augmented Plane Wave + Local Orbitals Program for Calculating Crystal Properties* (Karlheinz Schwarz, Tech. Universität Wien, Austria, 2001).
[32] J. P. Perdew, K. Burke, and M. Ernzerhof, Phys. Rev. Lett. **77**, 3865 (1996).
[33] S. K. Mishra, S. Satpathy, and O. Jepsen, J. Phys. Condens. Matter **9**, 461 (1997).
[34] O. V. Yazyev, J. E. Moore, and S. G. Louie, Phys. Rev. Lett. **105**, 266806 (2010).
[35] H. Jin, J.-H. Song, and A. J. Freeman, Phys. Rev. B **83**, 125319 (2011).
[36] S. Kim, M. Ye, K. Kuroda, Y. Yamada, E. E. Krasovskii, E. Chulkov, K. Miyamoto, M. Nakatake, T. Okuda, Y. Ueda *et al.*, Phys. Rev. Lett. **107**, 056803 (2011).
[37] V. Yazyev, E. Kioupakis, J. E. Moore, and S. G. Louie, e-print arXiv:1108.2088.
[38] R. W. G. Wyckoff, *Crystal Structures*, Vol. 2 (John Wiley & Sons, New York, 1964).
[39] J. P. Perdew, A. Ruzsinszky, G. I. Csonka, O. A. Vydrov, G. E. Scuseria, L. A. Constantin, X. Zhou, and K. Burke, Phys. Rev. Lett. **100**, 136406 (2008).
[40] J. Linder, T. Yokoyama, and A. Sudbø, Phys. Rev. B **80**, 205401 (2009).
[41] C.-X. Liu, H. Zhang, B. Yan, X.-L. Qi, T. Frauenheim, X. Dai, Z. Fang, and S.-C. Zhang, Phys. Rev. B **81**, 041307(R) (2010).
[42] H.-Z. Lu, W.-Y. Shan, W. Yao, Q. Niu, and S.-Q. Shen, Phys. Rev. B **81**, 115407 (2010).
[43] Y. Sakamoto, T. Hirahara, H. Miyazaki, S. Kimura, and S. Hasegawa, Phys. Rev. B **81**, 165432 (2010).
[44] Y. Zhang, K. He, C.-Z. Chang, C.-L. Song, L.-L. Wang, X. Chen, J.-F. Jia, Z. Fang, X. Dai, W.-Y. Shan *et al.*, Nature Phys. **6**, 584 (2010).
[45] K. Park, J. J. Heremans, V. Scarola, and D. Minic, Phys. Rev. Lett. **105**, 186801 (2010).